RSC Advances

PAPER

View Article Online
View Journal | View Issue

Cite this: *RSC Adv.*, 2017, **7**, 453

3D urchin-like black TiO_{2-x}/carbon nanotube heterostructures as efficient visible-light-driven photocatalysts

Yuchi Zhang,[a] Zipeng Xing,*[a] Jinlong Zou,[a] Zhenzi Li,[b] Xiaoyan Wu,[b] Liyan Shen,[a] Qi Zhu,[a] Shilin Yang*[a] and Wei Zhou*[a]

Received 21st October 2016
Accepted 9th November 2016

DOI: 10.1039/c6ra25611b

www.rsc.org/advances

3D urchin-like black TiO_{2-x}/CNT heterostructures are successfully fabricated *via* a facile one-pot solvothermal reaction combined with a subsequent *in situ* solid-state chemical reduction approach. The as-prepared photocatalysts are characterized in detail *via* X-ray diffraction, Raman spectroscopy, Fourier transform infrared spectroscopy, scanning electron microscopy, transmission electron microscopy, X-ray photoelectron spectroscopy and UV-vis diffuse reflectance spectroscopy. The results demonstrate that the obtained black TiO_{2-x}/CNT heterostructures exhibit a 3D urchin-like heterojunction structure, and Ti^{3+} is doped into the lattice of anatase TiO_2. This unique 3D structure with abundant active sites can enhance light scattering capability, and the Ti^{3+} self-doping defective TiO_2 with a narrow bandgap can promote visible-light photocatalytic activity. Therefore, the TiO_{2-x}/CNT heterostructures exhibit unparalleled high visible-light-driven photocatalytic activity and electrochemical properties. The visible-light-driven photocatalytic degradation rate for methylene orange is up to 99.6% and the hydrogen production rate is as high as 242.9 μmol h^{-1} g^{-1}, which is ascribed to the 3D urchin-like structure offering abundant active sites, the heterostructures resulting in the separation of photogenerated charge carriers, and the Ti^{3+} self-doping narrowing the bandgap and favoring visible light absorption.

Introduction

In recent years, photocatalytic technology has aroused much interest due to its application in the degradation of organic pollutants, production of hydrogen, and reduction of CO_2 to renewable hydrocarbon solar fuels.[1–3] In addition, capacitors, lithium ion batteries and solar cells are being researched to solve the energy shortage.[4,5] Among the myriad of photocatalytic materials, TiO_2, which is one of the most suitable photocatalysts, has received widespread attention due to its low cost, innocuity, good stability and commercial availability.[6–8] Nevertheless, the unavoidable disadvantages of TiO_2 photocatalysts include being limited to the ultraviolet region of the absorption spectrum and rapid recombination of photogenerated electron–hole pairs.[9,10] These issues lead to low solar-light utilization by TiO_2 and reduce the photo-induced redox reaction.[11,12] Thus the key factor to preparing highly active TiO_2 is to enhance its visible-light energy conversion and suppress photogenerated electron–hole pairs recombination.

In order to enhance TiO_2 activity in the visible light region, different methods can be employed, including modification with transition metal additives, non-metals, rare earth metals, self-doping and sensitizers or combination with other semiconductors, *etc.*[13–15] Defects in materials often show prominent effects that could lead to substantial advancement in the scientific field.[16,17] Recently, structurally defective TiO_2 with Ti^{3+} self-doping has been developed to expand its absorbance in the visible-light region.[18–21] Mao *et al.*[22] presented an innovative method to prepare TiO_2 with Ti^{3+} self-doping using the high pressure hydrogenation of TiO_2 nanocrystals. The as-prepared hydrogenated TiO_2 was successful in narrowing the bandgap and enhancing photocatalytic activities. Subsequently, various researches are dedicated to this field. Several synthetic methods have been reported, such as high temperature, high pressure, hydrogenation,[23,24] plasma treatment,[25,26] and vacuum activation.[27,28] However, these harsh and costly methods are less suitable for practical application. Therefore, a simple synthesis is required to produce TiO_2 with Ti^{3+} self-doping under milder experimental conditions and within shorter reaction times, in order to improve photocatalytic performances.

Coupling TiO_2 with other materials to form heterojunction structures is also an effective strategy to promote its photocatalytic activity. Carbon nanotubes (CNT) are one of the

[a]*Department of Environmental Science, School of Chemistry and Materials Science, Key Laboratory of Functional Inorganic Material Chemistry, Ministry of Education of the People's Republic of China, Heilongjiang University, Harbin 150080, P. R. China. E-mail: xzplab@163.com; ysl3000@126.com; zwchem@hotmail.com; Fax: +86-451-8660-8240; Tel: +86-451-8660-8616*

[b]*Department of Epidemiology and Biostatistics, Harbin Medical University, Harbin 150086, P. R. China*

numerous studied materials with the benefits of large surface areas, high conductivity, high chemical stability, high tensile strength, and unique one-dimensional (1D) structure.[29,30] At present, the reported synthetic methods for TiO_2/CNT composites are chemical vapour deposition, sol–gel, and the hydrothermal method, *etc.*[31–34] The application of TiO_2/CNT composites demonstrates the advantages of both materials, the photocatalytic activity of TiO_2, adsorption capacities of CNT and response of the prepared composites under visible-light irradiation. In addition, as 1D tubular structures, CNT can be synergized with TiO_2 nanoparticles to form a highly entangled three-dimensional (3D) urchin-like structure, which favors various technological applications including optical, electronic, and catalytic properties, because it results in more abundant active sites to enhance light trapping and scattering ability compared to what can be achieved with 1D and 2D nanostructured materials. Therefore, this type of system has been further researched in order to enhance the performance of photocatalysts.[35,36]

In this study, 3D urchin-like black TiO_{2-x}/CNT heterojunctions are synthesized *via* a simple and effective one-pot solvothermal reaction combined with a subsequent *in situ* solid-state chemical reduction approach. The photocatalytic and electrochemical properties of the prepared photocatalyst have been proven by the photocatalytic degradation of a contaminant, photocatalytic hydrogen evolution and electrochemical measurements. In addition, the possible photocatalytic mechanism of the 3D urchin-like black TiO_{2-x}/CNT heterojunctions is also proposed. Moreover, we believe that this effort will stimulate further research in the photocatalytic field in the near future.

Experimental

Material synthesis

Preparation of 3D urchin-like TiO_2/CNT composites. Prior to TiO_2 coating, pristine CNT underwent acid treatment to remove metal catalysts as well as introduce carboxyl groups on the CNT surface to ease the coating process later. During acid treatment, 0.4 g of CNT was stirred in a mixture of nitric acid and sulphuric acid mixed at a volume ratio of 1 : 3, each at the concentration of 5 M, under reflux at 100 °C for 180 min. Subsequently, 0.1 g of acid-treated CNT was dispersed in 50 mL of dehydrated alcohol with sonication for 30 min, and then 10 mL of glycerol and 1 mL of tetrabutyl titanate (TBT) were added into the prepared solution and gently stirred for 10 min. The mixture was then transferred to a 100 mL Teflon-lined stainless steel autoclave and kept in an electric oven at 180 °C for 15 h. The resulting powder was washed with ethanol and dried at 60 °C overnight, followed by calcination at 450 °C in air for 120 min, which is denoted as TiO_2/CNT.

Preparation of 3D urchin-like black TiO_{2-x}/CNT composites. At room temperature (20 °C ± 2 °C), 0.5 g of the above prepared sample was mixed with 1.0 g of sodium boron hydride ($NaBH_4$) and ground for 30 min thoroughly. Then, the mixture was transferred into porcelain boats, and placed in a tubular furnace to anneal at 350 °C under an Ar atmosphere at a heating rate of 5 °C min^{-1} from room temperature to 350 °C for 1 h. After cooling naturally to room temperature, the TiO_{2-x}/CNT composite was obtained (Fig. 1), which was simply washed with deionized water and absolute ethanol several times to remove unreacted $NaBH_4$, and dried at 60 °C. For comparison, TiO_{2-x} and the 3D urchin-like TiO_2/CNT composites were synthesized under the same conditions in the absence of CNT and $NaBH_4$, respectively.

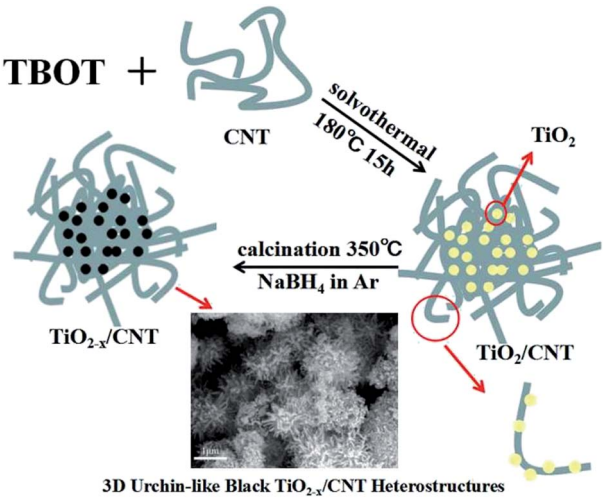

Fig. 1 Schematic of the formation of the TiO_{2-x}/CNT composites.

Characterization

X-ray diffraction (XRD) (Bruker D8 Discover) with a Cu K radiation wavelength of 1.54056 nm was used to determine the crystallographic properties of the nanocomposites. Raman measurements were performed with a Jobin Yvon HR 800 micro-Raman spectrometer at 457.9 nm. Fourier transform infrared spectra (FT-IR) of the samples, with KBr as diluents, were collected with a PerkinElmer Spectrum One system. Field-emission scanning electron microscopy (FE-SEM, Hitachi SU8010) was employed to observe the surface morphology of the ternary nanocomposites. Transmission electron microscopy (TEM) on a JEOL JEM-2010 at an accelerating voltage of 200 kV was applied to record electron micrographs of the samples. X-ray photoelectron spectroscopy (XPS) was carried out on a PHI-5700 ESCA with an Al Kα X-ray source. All binding energies were calibrated with surface adventitious carbon of 284.6 eV. UV-vis diffuse reflectance spectra (DRS) were obtained on a TU-1901 spectrophotometer using $BaSO_4$ as the background over the range of 190–800 nm.

Photocatalytic degradation

The liquid phase photodegradation of methyl orange (MO) was used as a probe to evaluate the catalytic performance of the samples and activity tests were carried out at room temperature in air. Before the photocatalytic reaction, 0.05 g samples were dispersed in 50 mL MO (10 mg L^{-1}) aqueous solution and magnetically stirred for 30 min in dark to achieve adsorption equilibrium. Then, the solution was placed in a 100 mL

cylindrical quartz reactor equipped with a water circulation facility under visible-light irradiation. A 300 W xenon lamp with a cut-off filter ($\lambda \geq 420$ nm) served as a visible-light source. At regular irradiation time intervals, the suspension liquid was sampled (5 mL) and centrifuged to separate the suspended catalyst. MO concentration was monitored using a UV-vis spectrophotometer at its characteristic wavelength ($\lambda = 554$ nm), from which the degradation ratio could be calculated.

Photocatalytic hydrogen evolution

Photocatalytic hydrogen evolution tests were carried out in an online photocatalytic hydrogen generation system (AuLight, Beijing, CEL-SPH2N) at room temperature. With Pt as the co-catalyst and 20 mL of methanol sacrificial agent, using a magnetic stirrer, 50 mg of photocatalysts were mixed with 80 mL of deionized water in a closed-gas circulation reaction cell. Prior to the reaction, the system was vacuumized completely to remove O_2 and CO_2 dissolved in water. Subsequently, the mixture solution was irradiated by a 300 W Xeon-lamp with a 420 nm cut-off filter. Using an on-line gas chromatograph, the hydrogen was periodically analyzed at an interval of 1 h (SP7800, TCD, molecular sieve 5 Å, N_2 carrier, Beijing Keruida, Ltd).

Electrochemical properties

The electrochemical properties of the catalysts were analyzed using the three-electrode cell configuration with a platinum counter electrode and standard calomel reference electrode at room temperature. An aqueous solution of 1 mol L^{-1} NaOH served as the electrolyte. An electrochemical workstation was employed to measure the photocurrent intensity of the samples under intermittent illumination with a 300 W Xe lamp (Perfectlife, PLS-SXE-300). The wavelength was over 300 nm and the irradiance was 176 mW cm^{-2}, as measured by a radiometer (FZ-A, Photoelectric Instrument Factory of Beijing Normal University). Electrochemical impedance spectroscopic (EIS) measurements were performed between 100 kHz and 0.01 Hz at 0.05 V under illumination.

Results and discussion

The X-ray diffraction patterns of the as-prepared samples are presented in Fig. 2. All the XRD patterns exhibit similar diffraction peaks except CNT, which appear at 25.3, 37.8, 48.1, 54.1, 54.9, 62.7, 68.9, 70.2, and 75.1. Compared with the standard pattern (JCPDS no. 21-1272), the as-prepared samples can be identified as anatase TiO_2. The above perks correspond to the crystal planes of (101), (004), (200), (105), (211), (204), (116), (220), and (215).[37] No characteristics peaks of CNT are found in the spectra of the composites in the range investigated. This may be attributed to the overlap of the intense peaks of the CNT (002) and anatase (001) reflections, and the difference in mass between CNT and TiO_2 is relatively large.[38] Moreover, TiO_{2-x}/CNT still keeps the anatase TiO_2 lattice plane after treatment with $NaBH_4$, however the diffraction peaks are evidently broadened and their intensity decreases, which indicate that its crystalline structure has some variations. According to related

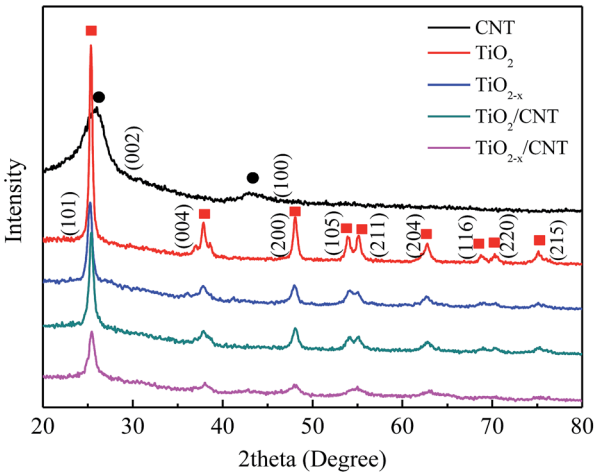

Fig. 2 XRD patterns of CNT, TiO_2, TiO_{2-x}, TiO_2/CNT, and TiO_{2-x}/CNT, respectively.

reports, the change in crystalline structure may be ascribed to the production of Ti^{3+} and oxygen vacancies through the chemical reduction treatment.[39]

Raman spectroscopy is another powerful tool to characterize both TiO_2 and CNT. As shown in Fig. 3, the Raman spectra of the composite sample exhibit characteristic peaks of anatase TiO_2 as well as the G- and D-bands of CNT. Four vibrational modes with strong intensities at 142 (E_g), 396 (B_{1g}), 517 (B_{1g} + A_{1g}), and 639 cm^{-1} (E_g) are observed, which reveal that anatase is the predominant phase of the pure TiO_2 particles.[40] In addition, these peaks, although shift toward higher frequencies, also appear in the TiO_2/CNT and the TiO_{2-x}/CNT composites, and such changes can be reasonably attributed to the interaction between TiO_2 and CNT.[41] Two characteristic peaks appear in the composite and pure CNT at wavelengths of approximately 1353 and 1586 cm^{-1}, which correspond to the disordered carbon (D band) and graphitic carbon (G band) of the CNT,

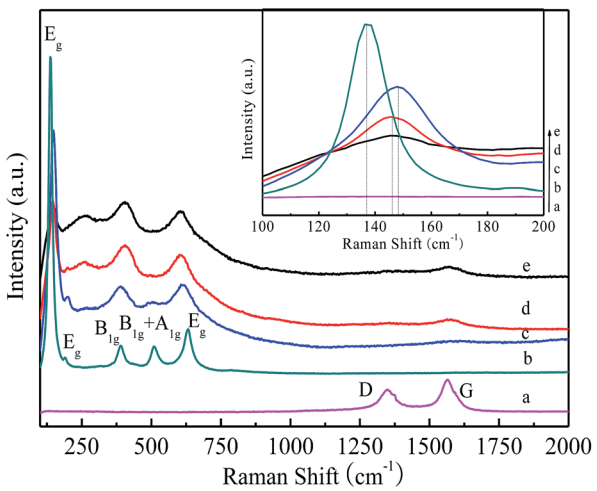

Fig. 3 Raman spectra of CNT (a), TiO_2 (b), TiO_{2-x} (c), TiO_2/CNT (d) and TiO_{2-x}/CNT (e). The inset is the magnified E_g mode of the samples between 100–200 cm^{-1}.

respectively. Moreover, TiO_{2-x} exhibits blue-shifting compared to the pure TiO_2, and broadening and weakening of the E_g peak, which are attributed to the formation of Ti^{3+} and oxygen deficiencies in the TiO_2 lattice,[42] and are consistent with the XRD results.

FT-IR was used to investigate the functional groups of the as-synthesized samples. Fig. 4 shows the IR spectra of the samples collected in the region of 400–4000 cm^{-1}. All the samples present similar spectra in which a strong absorption peak appears in the range of 400–800 cm^{-1} except CNT, which can be mainly ascribed to the Ti–O–Ti flexion vibration.[43] The signals in the region of 1400–1630 cm^{-1} in the hybrid confirm the presence of CNT and indicate that the polymer removal process does not produce any apparent damage to the CNT. The functional groups of C=C (1476 cm^{-1} and 1569 cm^{-1}) and C=O (1670 cm^{-1}) were found in the prepared composite, which are the characteristic functional groups of CNT. Furthermore, the FT-IR peaks at about 3348 cm^{-1} are ascribed to the stretching vibrations of surface hydroxyl groups.[44] The observed functional groups of TiO_2 and CNT indicate that the hybrid structures were successfully obtained by the one-pot solvothermal reaction.

Fig. 5 shows SEM images of the samples. As shown in Fig. 5a, a 3D flower-liked structure is exhibited, which reflects the aggregation effect of pure TiO_2. The surface morphology of the TiO_{2-x}/CNT composites is shown in Fig. 5c and d. Pure CNT had a smooth surface and homogeneous dispersion (Fig. 5b), and the TiO_2 nanoparticles were deposited over the surface of CNT. No individual and isolated TiO_2 nanomaterial was evidently observed in the TiO_{2-x}/CNT composite. Fig. 5c displays the highly entangled 3D urchin-like architecture formed by the synergistic effect of CNT and TiO_2, and Fig. 5d reveals its surface morphology, which features the assembly of CNT in different angles with TiO_2 nanoparticles. These well designed TiO_{2-x}/CNT composites can greatly increase surface area, promote light scattering, and thus improve the photocatalytic performance.

Transmission electron microscopy analysis was used to investigate the crystal structure and morphology of the samples. The TEM and HRTEM images of the TiO_{2-x}/CNT composite are shown in Fig. 6. As shown in Fig. 6a and b, the 3D urchin-like structure is also exhibited, which is consistent with the SEM image. Fig. 6c and d show the HRTEM image of the TiO_{2-x}/CNT composite structure. The high magnification image (Fig. 6c) discloses the lattice fringes of TiO_2 and CNT. The lattice spacing of 0.35 nm obtained from the TiO_2 nanoparticles is attributed to the crystal facet of (101).[24] Moreover, the lattice spacing of 0.34 nm is identical to the facet of (002) of CNT. Fig. 6d shows TiO_2 nanoparticles deposited on the tube wall of the CNT. The heterojunction of the CNT–TiO_2 (highlighted area in Fig. 6d) can be visualized from the overlapping of the two different lattice fringes of CNT and TiO_2. The CNT–TiO_2 heterojunction would promote electron transfer and separation, thus promoting photocatalytic reactions.[45]

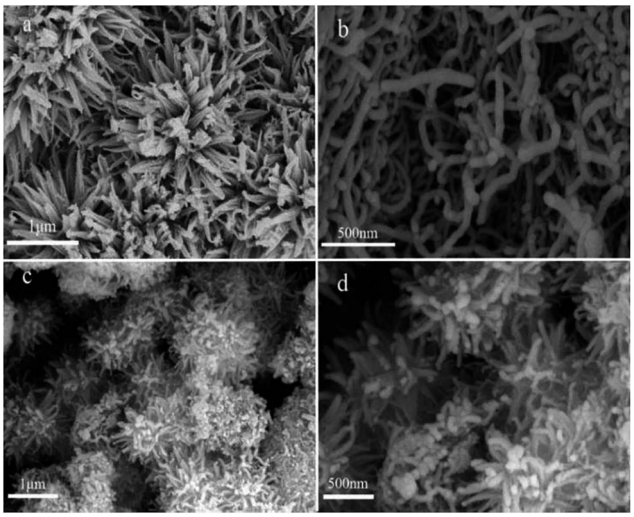

Fig. 5 SEM images of TiO_2 (a), CNT (b), and TiO_{2-x}/CNT composite (c, d).

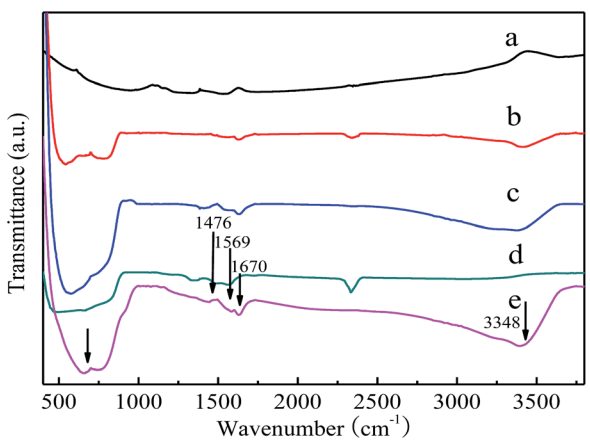

Fig. 4 FT-IR spectra of CNT (a), TiO_2 (b), TiO_{2-x} (c), TiO_2/CNT (d) and TiO_{2-x}/CNT (e).

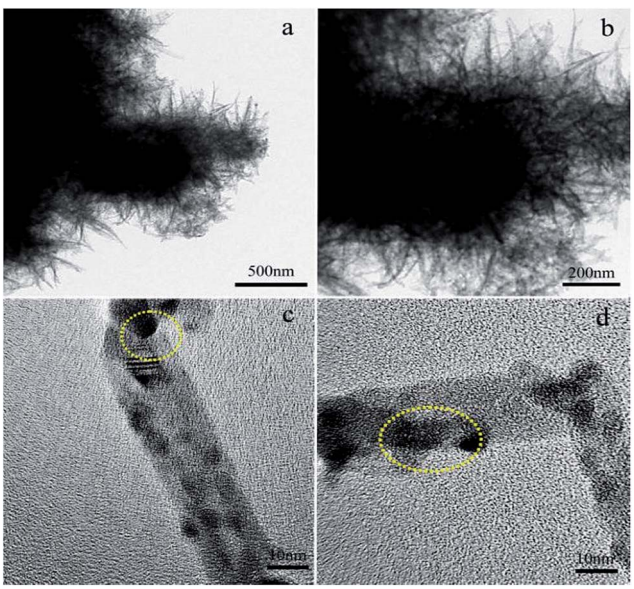

Fig. 6 TEM (a, b) and HRTEM images (c, d) of the TiO_{2-x}/CNT composite.

X-ray photoelectron spectroscopy was used to characterize the TiO_{2-x}/CNT composite. The chemical state and surface composition of TiO_{2-x}/CNT are shown in Fig. 7. Fig. 7a presents the full-scale XPS spectrum of TiO_{2-x}/CNT, which indicates the existence of Ti, O and C elements. Fig. 7b presents the Ti 2p region, and the bands centered at 457.84, 458.43, 463.54 and 464.11 eV correspond to Ti^{3+} $2p_{3/2}$, Ti^{4+} $2p_{3/2}$, Ti^{3+} $2p_{1/2}$, and Ti^{4+} $2p_{1/2}$, respectively. Ti^{3+} species are created due to the Ti^{4+} reduction of TiO_2 in the process of treatment with $NaBH_4$. Fig. 7c presents the O 1s region, which is asymmetric and deconvoluted into two peaks. The main peak at 530.43 eV can be ascribed to lattice oxygen (O_2^{2-}) in anatase TiO_2, whereas the broad peak at 531.87 eV is assigned to C=O or Ti–O–C bonds.[46] The corresponding C 1s spectrum in Fig. 7d can also be deconvoluted into four peaks. The peak at 283.81 eV can be ascribed to the sp^2 carbon.[47] The peak at 284.80 eV is attributed to adventitious carbon and sp^3 carbon from CNT. The peaks at 286.02 and 288.71 eV correspond to O–C=O[33,48] from the functional groups on CNT, which may act as the anchoring center for the nucleation of TiO_2, thus forming O=C–Ti or C–O–Ti bands.

The UV-vis diffuse reflectance spectra of the four investigated photocatalysts are shown in Fig. 8. As shown in Fig. 8a, the as-prepared TiO_{2-x} sample exhibits a stronger absorption between 400–800 nm compared to pure TiO_2. This strong absorption in the visible-light region is attributed to the existence of bulk Ti^{3+} defects, which induces a continuous vacancy band of electronic states just below the conduction band edge of TiO_{2-x}. In addition, the light absorption of the TiO_2/CNT composite is found to have a similar trend with that of the anatase TiO_2, but at a magnified scale with absorption in the visible light range (400–800 nm). This observation suggests that modification of TiO_{2-x}/CNT could provide efficient visible-light-driven photocatalytic activity, thus enhancing electron–hole pair generation under visible light irradiation, which further contributes to enhanced photocatalytic performance.[31,49] Using the Kubelka–Munk function as the vertical axis against photon energy, as shown in Fig. 8b, the band gap of TiO_2 and TiO_{2-x} is 3.08 and 2.46, respectively. These results suggest that TiO_{2-x} is more active with a narrower intrinsic band gap than the as-prepared TiO_2 catalysts. Moreover, the narrow band gap is beneficial for visible-light-driven photocatalysis.

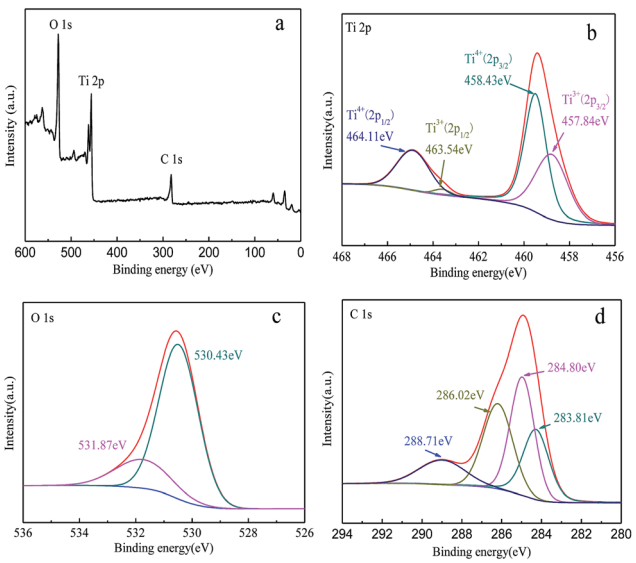

Fig. 7 Full-scale XPS spectra of TiO_{2-x}/CNT (a), Ti 2p (b), O 1s (c), and C 1s (d).

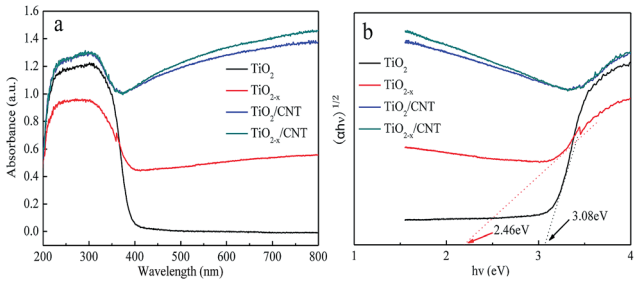

Fig. 8 UV-vis spectra (a) with different samples, and determination of the indirect interband transition energies (b) for TiO_2 and TiO_{2-x}.

The photocatalytic activity of different samples was evaluated by the photodegradation of MO degradation under visible-light irradiation and the results are shown in Fig. 9. For comparison, a blank experiment without the presence of a catalyst was performed under visible-light irradiation. As shown in Fig. 9a, the self-degradation process by only 1.12% degraded MO can be neglected after 150 min of visible-light irradiation. After 30 min of dark adsorption equilibrium, the initial MO can be removed by 8.9%, 9.8%, 52.5%, and 53.9% with TiO_2, TiO_{2-x}, TiO_2/CNT, and TiO_{2-x}/CNT, respectively. These results show the excellent adsorption properties of CNT. In comparison to pure TiO_2, TiO_{2-x}, TiO_2/CNT, and TiO_{2-x}/CNT have excellent visible-light photocatalytic performances. In particular, TiO_{2-x}/CNT shows the highest catalytic activity, which reaches 99.6% of MO removal within 150 min of visible-light irradiation. Moreover, the obtained apparent rate constant, k, values of TiO_2, TiO_{2-x}, TiO_2/CNT, and TiO_{2-x}/CNT, as shown in the Fig. 9b, are 0.0006, 0.0043, 0.0010 and 0.0048 min^{-1}, respectively. Identically, the TiO_{2-x}/CNT also shows the highest value around 8 times higher than that of pristine TiO_2. This new photocatalyst shows better photocatalytic activity than that reported in previous literatures,[50,51] which is attributed to the Ti^{3+} self-doping and 3D urchin-like structure.

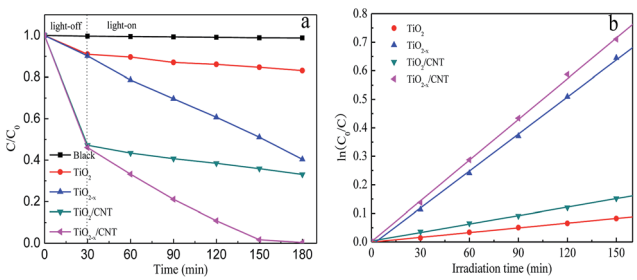

Fig. 9 Photocatalytic activity with the different samples under visible-light irradiation (a), and variations of $\ln(C_0/C)$ *versus* visible-light irradiation time with the different samples (b).

To further demonstrate the excellent photocatalytic performance of TiO_{2-x}/CNT, the photocatalytic hydrogen evolution rate under simulated solar light (AM 1.5) irradiation was also tested through the photocatalytic hydrogen production process.[52,53] In Fig. 10a, the pure TiO_2 and CNT show poor photocatalytic hydrogen evolution activity. However, TiO_{2-x}, TiO_2/CNT, and TiO_{2-x}/CNT can be excited under visible-light to give hydrogen evolution rates of 125.13, 101.54 and 242.91 μmol h^{-1} g^{-1}, respectively. These results reveal that the introduction of Ti^{3+} and the effect of the 3D urchin-like heterojunction structure play significant roles in the process of hydrogen generation. Fig. 10b shows the recycling hydrogen evolution reaction used to examine the photocatalytic stability of TiO_{2-x}/CNT. The H_2 evolution rates remain almost constant after five cycles lasting 25 h, which indicates the high stability of the TiO_{2-x}/CNT composite.

Electrochemical impedance spectroscopy (EIS) was conducted to investigate the interfacial electrical properties between electrodes and solutions. The diameters of the semicircles are equal to the charge-transfer resistance of a sample, and the tail in the low frequency region represents the diffusion process of ions in the electrode materials. Based on previous studies, a smaller semicircle diameter implies more effective separation of the photogenerated e–h pairs and/or a faster interfacial charge transfer to the electron donor–acceptor.[48,54] Fig. 11 shows the Nyquist curves of pure TiO_2, TiO_{2-x}, TiO_2/CNT, and TiO_{2-x}/CNT photocatalysts. It can clearly be seen that the semicircle for TiO_{2-x}/CNT is much smaller than that of the others. Similarly, the photocatalytic activity of TiO_{2-x} is stronger than that of pristine TiO_2. This implies that CNT and Ti^{3+} play an important role in improving the conductivity of the composite, which improves the rate capability of the electrode. In addition, the 3D urchin-like heterojunction structures also contribute to a decrease in the charge transfer resistance and

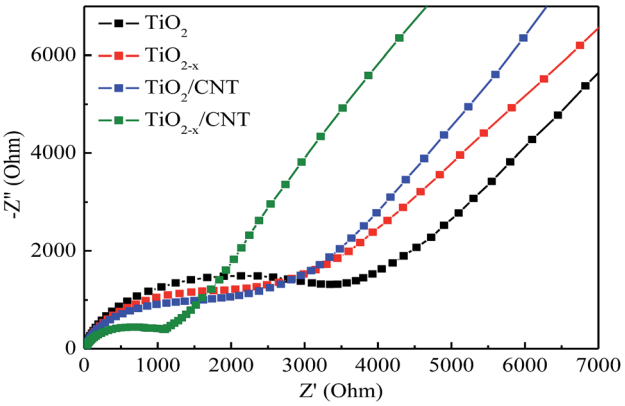

Fig. 11 Nyquist plots for TiO_2, TiO_{2-x}, TiO_2/CNT and TiO_{2-x}/CNT.

charge recombination, and thus result in improved electrochemical properties.[55–57]

The electron charge transfer mechanism during the photoexcitation of the composites was investigated and is proposed in Fig. 12. Ti^{3+} and oxygen vacancy are introduced in the conduction band (CB) of TiO_2, which narrow the band gap and enhance the visible-light absorption. Therefore, the electrons in the valence band (VB) can easily transfer to the CB of TiO_2 under visible-light irradiation. Furthermore, CNT with their unique properties play an important role in improving the electron charge transfer efficiency during visible-light irradiation. The strong interaction between CNT and TiO_2 allows the migration of electrons from TiO_2 to CNT, which consequently reduces the chance of electron–hole recombination and accelerates the formation of superoxide anion radicals ($^{\bullet}O_2^-$). These processes can lead indirectly to the generation of $^{\bullet}OH$ radicals. $^{\bullet}OH$ and $^{\bullet}O_2^-$ with strong oxidation ability can cause the degradation of organic pollutants. In addition, the excited electrons in the CB on the surface can reduce H^+ ions for the evolution of H_2. Therefore, the photocatalytic hydrogen production capacity of the photocatalyst is also improved.

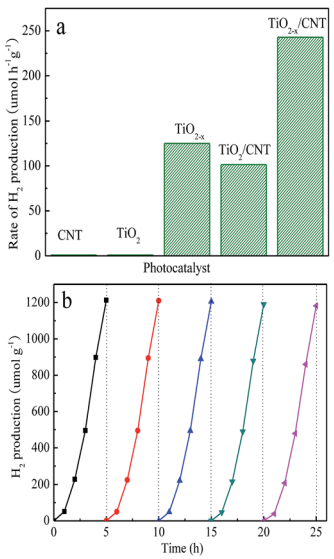

Fig. 10 Photocatalytic hydrogen evolution for the different samples under AM 1.5 irradiation (a), and recyclability of TiO_{2-x}/CNT for H_2 evolution under AM 1.5 irradiation (b).

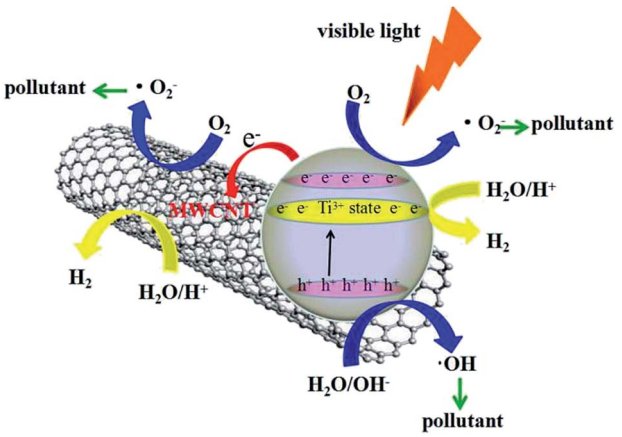

Fig. 12 Schematic of the visible-light-driven photocatalytic mechanism for the TiO_{2-x}/CNT composite.

Conclusions

In conclusion, a 3D urchin-like black TiO_{2-x}/CNT structured photocatalyst was successfully developed *via* a facile one-pot solvothermal method. Under visible-light irradiation, the results show that the prominently improved photocatalytic activity and electrochemical properties were direct consequences of the urchin-like heterojunction structure and Ti^{3+} species in the frameworks. The 3D urchin-like black TiO_{2-x}/CNT has the highest MO degradation ratio, H_2 evolution, and conductivity compared with pristine TiO_2, TiO_{2-x}, TiO_2/CNT, and TiO_{2-x}/CNT. In particular, MO could be photocatalytically degraded completely by TiO_{2-x}/CNT heterojunctions in 150 min under visible-light irradiation, and a hydrogen evolution rate of 242.91 μmol h^{-1} g^{-1} could be achieved. The excellent photocatalytic activity and electrochemical property of TiO_{2-x}/CNT is ascribed to the synergistic effect of CNT composited TiO_2, Ti^{3+} self-doping, and the 3D urchin-like heterojunction structure. The prepared novel 3D urchin-like heterojunction photocatalyst will provide a new insight for the rational design of other functional materials and contribute to solve the increasing environmental pollution puzzles.

Acknowledgements

We gratefully acknowledge the support to this research by the National Natural Science Foundation of China (21376065, 81302511, 81573134, 21106035 and 51672073), the Natural Science Foundation of Heilongjiang Province (QC2012C001, QC2013C079 and E201456), the Heilongjiang Postdoctoral Startup Fund (LBH-Q14135), the Program for New Century Excellent Talents in University of Heilongjiang Province (1253-NCET-020), the University Nursing Program for Young Scholars with Creative Talents in Heilongjiang Province (UNPYSCT-2015014) and the Youth Science and Technology Innovation Talent Program in Education Department of Heilongjiang Province (UNPYSCT-2016018).

Notes and references

1 J. Ran, J. Zhang, J. Yu, M. Jaroniec and S. Z. Qiao, *Chem. Soc. Rev.*, 2014, **43**, 7787.
2 Z. Xing, W. Zhou, F. Du, Y. Qu, G. Tian, K. Pan, C. Tian and H. Fu, *Dalton Trans.*, 2014, **43**, 790.
3 L. Zhang, Z. Xing, H. Zhang, Z. Li, X. Wu, X. Zhang, Y. Zhang and W. Zhou, *Appl. Catal., B*, 2016, **180**, 521.
4 I. Y. Jeon, M. J. Ju, J. Xu, H. J. Choi, J. M. Seo, M. J. Kim, I. T. Choi, H. M. Kim, J. C. Kim, J. J. Lee, H. K. Liu, H. K. Kim, S. Dou, L. Dai and J. B. Baek, *Adv. Funct. Mater.*, 2015, **25**, 1170.
5 S. Li, Y. Luo, W. Lv, W. Yu, S. Wu, P. Hou, Q. Yang, Q. Meng, C. Liu and H. M. Cheng, *Adv. Energy Mater.*, 2011, **1**, 486.
6 C. Dinh, H. Yen, F. Kleitz and T. Do, *Angew. Chem., Int. Ed.*, 2014, **53**, 6618.
7 S. Ullah, E. P. Ferreira-Neto, A. A. Pasa, C. C. J. Alcântara, J. J. S. Acuna, S. A. Bilmes, M. L. M. Ricci, R. Landers, T. Z. Fermino and U. P. Rodrigues-Filho, *Appl. Catal., B*, 2015, **179**, 333.
8 X. Liu, G. Dong, S. Li, G. Lu and Y. Bi, *J. Am. Chem. Soc.*, 2016, **138**, 2917.
9 Z. Xing, J. Li, Q. Wang, W. Zhou, G. Tian, K. Pan, C. Tian, J. Zou and H. Fu, *Eur. J. Inorg. Chem.*, 2013, **2013**, 2411.
10 G. Y. Yu, W. Zhang, Y. Sun, T. Xie, A. Ren, X. Zhou and G. Liu, *J. Mater. Chem. A*, 2013, 1.
11 N. Liu, V. Haublein, X. Zhou, U. Venkatesan, M. Hartmann, M. Mackovic, T. Nakajima, E. Spiecker, A. Osvet, L. Frey and P. Schmuki, *Nano Lett.*, 2015, **15**, 6815.
12 Z. Xing, W. Zhou, F. Du, L. Zhang, Z. Li, H. Zhang and W. Li, *ACS Appl. Mater. Interfaces*, 2014, **6**, 16653.
13 J. Dong, J. Han, Y. Liu, A. Nakajima, S. Matsushita, S. Wei and W. Gao, *ACS Appl. Mater. Interfaces*, 2014, **6**, 1385.
14 K. Hemalatha, A. S. Prakash, K. Guruprakash and M. Jayakumar, *J. Mater. Chem. A*, 2014, **2**, 1757.
15 M. Ge, C. Cao, J. Huang, S. Li, Z. Chen, K. Zhang, S. S. Al-Deyab and Y. Lai, *J. Mater. Chem. A*, 2016, **4**, 6772.
16 W. Zhou, F. Sun, K. Pan, G. Tian, B. Jiang, Z. Ren, C. Tian and H. Fu, *Adv. Funct. Mater.*, 2011, **21**, 1922.
17 V. Etacheri, M. K. Seery, S. J. Hinder and S. C. Pillai, *Adv. Funct. Mater.*, 2011, **21**, 3744.
18 J. Eom, S. Lim, S. Lee, W. Ryu and H. Kwon, *J. Mater. Chem. A*, 2015, **3**, 11183.
19 K. K. Adepalli, M. Kelsch, R. Merkle and J. Maier, *Adv. Funct. Mater.*, 2013, **23**, 1798.
20 X. Y. Pan, M. Q. Yang, X. Z. Fu, N. Zhang and Y. J. Xu, *Nanoscale*, 2013, **5**, 3601.
21 S. M. Prokes, J. L. Gole, X. B. Chen, C. Burda and W. E. Carlos, *Adv. Funct. Mater.*, 2005, **15**, 161.
22 X. Chen, L. Liu, P. Y. Yu and S. S. Mao, *Science*, 2011, **331**, 746.
23 J. Y. Shin, J. H. Joo, D. Samuelis and J. Maier, *Chem. Mater.*, 2012, **24**, 543.
24 A. Naldoni, M. Allieta, S. Santangelo, M. Marelli, F. Fabbri, S. Cappelli, C. L. Bianc-hi, R. Psaro and V. D. Santo, *J. Am. Chem. Soc.*, 2012, **134**, 7600.
25 C. Tang, L. Liu, Y. Li and Z. Bian, *Appl. Catal., B*, 2016, **16**, 0926.
26 C. Yang, Z. Wang, T. Lin, H. Yin, X. Lu, D. Wan, T. Xu, C. Zheng, J. Lin, F. Huang, X. Xie and M. Jiang, *J. Am. Chem. Soc.*, 2013, **135**, 17831.
27 T. Lin, C. Yang, Z. Wang, H. Yin, X. Lv, F. Huang, J. Lin, X. Xie and M. Jiang, *Energy Environ. Sci.*, 2014, **7**, 967.
28 Y. Yan, J. Miao, Z. Yang, F. Xiao, H. Yang, B. Liu and Y. Yang, *Chem. Soc. Rev.*, 2015, **44**, 3295.
29 Z. Wang, C. Yang, T. Lin, H. Yin, P. Chen, D. Wan, F. Xu, F. Huang, J. Lin, X. Xie and M. Jiang, *Energy Environ. Sci.*, 2013, **6**, 3007.
30 Q. Zhang, J. Huang, W. Qian, Y. Zhang and F. Wei, *Small*, 2013, **9**, 1237.
31 H. Zhou, L. Liu, X. Wang, F. Liang, S. Bao, D. Lv, Y. Tang and D. Jia, *J. Mater. Chem. A*, 2013, **1**, 8525.
32 N. G. Akalework, C. Pan, W. Su, J. Rick, M. C. Tsai, J. F. Lee, J. M. Lin, L. D. Tsai and B. J. Hwang, *J. Mater. Chem.*, 2012, **22**, 20977.

33 K. Hemalatha, P. M. Ette, G. Madras and K. Ramesha, *J. Sol-Gel Sci. Technol.*, 2015, **73**, 72.
34 M. Gui, S. Chai, B. Xu and A. R. Mohamed, *Sol. Energy Mater. Sol. Cells*, 2014, **122**, 183.
35 K. Fan, T. Peng, J. Chen, X. Xiao and R. Li, *J. Power Sources*, 2013, **222**, 38.
36 Z. He, J. Liu, J. Miao, B. Liu and T. Tan, *J. Mater. Chem. C*, 2014, **2**, 1381.
37 J. Huo, Y. Hu, H. Jiang and C. Li, *Nanoscale*, 2014, **6**, 9078.
38 Z. Chena, Z. Mab, J. Songb and L. Wang, *J. Power Sources*, 2016, **324**, 86.
39 W. Zhou, W. Li, J. Wang, Y. Qu, Y. Yang, Y. Xie, K. Zhang, L. Wang, H. Fu and D. Zhao, *J. Am. Chem. Soc.*, 2014, **136**, 9280.
40 N. Li, G. Liu, C. Zhen, F. Li, L. Zhang and H. Cheng, *Adv. Funct. Mater.*, 2011, **21**, 1717.
41 X. Liao, R. Gerdts, S. F. Parker, L. Chi, Y. Zhao, M. Hill, J. Guo, M. O. Jones and Z. Jiang, *Phys. Chem. Chem. Phys.*, 2016, **18**, 17311.
42 W. Hu, W. Zhou, K. Zhang, X. Zhang, L. Wang, B. Jiang, G. Tian, D. Zhao and H. Fu, *J. Mater. Chem. A*, 2016, **4**, 7495.
43 B. Xia, S. Ding, H. Wu, X. Wang and X. Lou, *RSC Adv.*, 2012, **2**, 792.
44 R. R. N. Marques, B. F. Machado, J. L. Faria and A. M. T. Silva, *Carbon*, 2010, **48**, 1515.
45 J. Di, Z. Yong, Z. Yao, X. Liu, X. Shen, B. Sun, Z. Zhao and H. He, *Small*, 2013, **9**, 148.
46 J. Wang, R. Ran, M. O. Tade and Z. P. Shao, *J. Power Sources*, 2014, **254**, 18.
47 H. Ming, H. Huang, K. Pan, H. Li, Y. Liu and Z. Kang, *J. Solid State Chem.*, 2012, **192**, 305.
48 J. Yu, T. Ma and S. Liu, *Phys. Chem. Chem. Phys.*, 2011, **13**, 3491.
49 W. Hou and S. B. Cronin, *Adv. Funct. Mater.*, 2013, **23**, 1612.
50 B. Czech, W. Buda, S. P. Patkowska and P. Oleszczuk, *Appl. Catal., B*, 2015, **162**, 564.
51 C. Hung, C. Yuan and H. Li, *J. Hazard. Mater.*, 2017, **322**, 243.
52 L. Wang, X. Duan, G. Wang, C. Liu, S. Luo, S. Zhang, Y. Zeng, Y. Xu, Y. Liu and X. Duan, *Appl. Catal., B*, 2016, **186**, 88.
53 C. Liu, L. Wang, Y. Tang, S. Luo, Y. Liu, S. Zhang, Y. Zeng and Y. Xu, *Appl. Catal., B*, 2015, **164**, 1.
54 L. Huang, Q. Chan, X. Wu, H. Wang and Y. Liu, *J. Ind. Eng. Chem.*, 2012, **18**, 574.
55 G. Xi, J. Ye, Q. Ma, N. Su, H. Bai and C. Wang, *J. Am. Chem. Soc.*, 2012, **134**, 6508.
56 Z. Liu, J. Liu, J. Liu, L. Wang, G. Zhang and X. Sun, *Phys. Chem. Chem. Phys.*, 2014, **16**, 8808.
57 W. Ren, H. Zhang, D. Kong, B. Liu, Y. Yang and C. Cheng, *Phys. Chem. Chem. Phys.*, 2014, **16**, 22953.